ORIGINAL ARTICLE

Narrow gap welding of 316L thick-section steel with cold metal transition pulsed arc swing

Wei Meng[1,2] · Kai Chen[1] · Qinyue Pan[1] · Kai Ye[1] · Zhenhua Liu[1] · Qunshuang Ma[1] · Lei Hu[1,2] · Wenbo Du[1] · Xiaohui Yin[1,2]

Abstract

Narrow gap welding of 316L stainless steel thick plate was carried out using the cold metal transition pulsed wire-arc swing method. The effects of heat input, arc swing, and shielding mode on weld shaping and lack of fusion were investigated, and microstructure and tensile properties of welded joints were analyzed and characterized. The results indicate that arc swing amplitude was the primary factor affecting sidewall fusion. The tendency of undercut and incomplete fusion at the weld toe increased with the increase of wire feeding speed. Narrow gap weld with built-in shielding was easy to produce pores. The microstructure of welded joints was mostly represented by twin crystals in HAZ and columnar dendrites in the weld. Solidification sub-boundaries were produced between dendritic crystal clusters in the middle of the weld under high heat input, resulting in severe regional segregation and crystalline cracks that extended along subgrain boundaries. The microhardness of the weld and HAZ was greater than that of the base material. The tensile strength of welded joints was comparable to that of base material with good mechanical properties.

Keywords Narrow gap welding · Cold metal transition · Pulsed arc swing · Lack of fusion defect · Mechanical property

1 Introduction

With the development of thick-walled high-strength welded structures, thick plates are more and more widely used in the structural components of large-scale equipment such as ships, offshore platforms, bridges, pressure vessels, and nuclear [1–3]. The joining technique of thick plate in welding production is mainly multi-layer multi-pass welding, which can cause welding deformation, toughness deterioration, and low welding efficiency. Narrow gap welding, which combines multi-layer single-pass welding with narrow grooving, can successfully address these problems [4]. In comparison to the conventional welding process with a large groove, the narrow gap method has a small groove

gap, low heat input, and good joint performance, making it appropriate for stainless steel, high-strength steel, and various welding applications [5, 6]. As an efficient and high-quality thick plate metal welding technology, narrow gap welding will have a broader application prospect.

At present, common narrow gap welding methods include narrow gap gas tungsten arc welding (NG-GTAW), narrow gap gas metal arc welding (NG-GMAW), narrow gap submerged arc welding (NG-SAW), narrow gap laser welding (NG-LW), and electron beam welding (NG-EW), which are distinguished mainly by heat source and wire feeding method. NG-GTAW has the advantages of low heat input, arc stability, and applicability to multi-position welding, but the small molten pool makes it easy to produce infused sidewalls [7]. Narrow gap laser and electron beam self-melting or filler wire welding have a limited melting pool and poor process flexibility, making them unsuitable for high-quality welds in industrial applications [8, 9]. NG-GMAW is characterized by high efficiency, high deposition rate, and high adaptability, but its complex equipment and narrow process window make it highly susceptible to porosity and unfused defects [10, 11]. In recent years, the mechanisms of arc behavior, droplet transfer, and incomplete fusion defects

---

Wei Meng and Kai Chen are the co-first authors.

✉ Wei Meng
mengwei@ahut.edu.cn

1 School of Materials Science and Engineering, Anhui University of Technology, Ma'anshan 243032, China

2 Anhui Key Lab of Materials Science and Processing, Anhui University of Technology, Ma'anshan 243002, Anhui, China

in narrow gap welding have attracted more and more attention, but the development of new welding technology is rare [12, 13]. In contrast, in order to achieve high-quality narrow gap welding, it is necessary to combine low heat input heat source with high fusion efficiency. Thus, it is very important to develop narrow gap arc welding technology with high process flexibility and low heat input.

Cold metal transfer (CMT) welding is unrivaled in thin plate welding and fusion brazing due to its narrow heat-affected zone (HAZ), low distortion, and high productivity [14, 15]. The applicability of CMT welding technology is limited by its low heat input and small dilution rate, and various researchers have argued that it is not suitable for narrow gap welding [16]. Note that the CMT pulse process retains all the advantages of CMT welding and makes up for the lack of heat input of the CMT process. By adjusting the waveform of the output current, pulsed arc welding may flexibly change the distribution of arc energy. The CMT method can increase the fusion efficiency of narrow gap welding by introducing pulse current mode, which helps to compensate for the poor fusion ratio of CMT welding. Consequently, CMT pulse welding has the characteristics of low input heat and high fusion efficiency, and will have a better application prospect in narrow gap welding.

Narrow gap robotic GMA welding is an efficient approach for joining thick-walled materials because of its low filler material consumption, high efficiency, and good adaptability [17, 18]. Robot NG-GMAW is often used for thick plate welding. However, insufficient sidewall fusion is still the most common and basic problem in NG-GMAW welding, which is usually attributed to insufficient input heat and filling metal. Furthermore, wire deflection and extensive grooves might cause fusion failure [19, 20]. Li RY et al. [21] discovered that the groove gap had a direct impact on the fusing of the sidewalls. Due to the narrow gap of the NG-GMAW groove, it is difficult to heat the sidewall of the groove by arc. As a result, the key technology to achieve effective NG-GMAW is to ensure good fusion of groove sidewalls [22, 23]. At present, a variety of NG-GMAW technologies have been developed by researchers, including serpentine wire welding, rotary arc welding, double-wire welding, and swinging (or oscillating) arc welding [24]. In general, these methods require the use of specialized wire feeding equipment, and the adaptability of the welding process is limited. Despite the fact that numerous researchers [20, 23] have conducted extensive research on sidewall

infusion, this topic remains unresolved. Additionally, in the welding process, austenitic stainless steel frequently exhibits porosity and crystallization cracks, which will undoubtedly occur in the narrow gap welding procedure [25]. The employment of robotic arc swing narrow gap welding may achieve all-position welding of the workpiece and flexible adjustment of welding parameters, making narrow gap welding methods more popular and applicable. Therefore, it is necessary to use CMT pulsed arc narrow gap welding (NGW-CMT) to improve the welding quality of austenitic stainless steel thick plates and avoid defects such as incomplete fusion and cracks.

A study on the narrow gap welding of 316L stainless steel thick plate was conducted in this paper utilizing a self-developed robotic pulsed arc swing CMT narrow gap welding system. The effects of welding parameters and swing on the weld shaping and sidewall fusion characteristics of 316L thick plate narrow gap welding were investigated, microstructure evolution and metallurgical bonding mechanisms of welded joints were thoroughly analyzed, and the quality of narrow gap welded joints was assessed using tensile and hardness tests.

2 Experimental procedures

316L austenitic stainless steel commonly used in the nuclear power industry was selected for the welding experiments, and the dimensions (length × width × thickness) were $100 \times 50 \times 30$ mm^3. The microstructure of 316L steel plate consists of banded austenite distributed along the rolling direction and a small amount of strip δ-ferrite distributed along the grain boundary. The filler wire was ER 316L stainless steel with a diameter of 1.2 mm. The chemical compositions of base metal and welding wire are listed in Table 1.

Figure 1 shows a schematic diagram of the CMT narrow gap welding device and groove. As shown in Fig. 1a, an ABB welding robot and a CMT welder (CMT Advanced 4000 R nc) were used to execute narrow gap welding. NG-CMT welding position was a horizontal butt joint. Since the narrow gap welding adopts the "I" groove, the arc center cannot directly act on the sidewall, which is not conducive to the heating and melting of the sidewall metal. Compared with U-shaped and V-shaped grooves, the gap of the I-shaped groove is smaller. Thus, efficient welding of narrow gap grooves can be achieved with less heat input and

Table 1 Compositions of 316L base metal and ER316L filler wire (wt. %)

	Element						
	C	Si	Mn	Cr	Ni	Mo	Fe
316L	0.02	0.45	1.58	17.74	12.89	2.05	Bal
ER316L	0.02	0.78	1.89	18.71	12.32	2.3	Bal

Fig. 1 Experimental setup and procedure for narrow gap multi-layer welding: **a** CMT narrow gap welding equipment, **b** narrow gap welding process, **c** weld shaping and dimensioning in mm
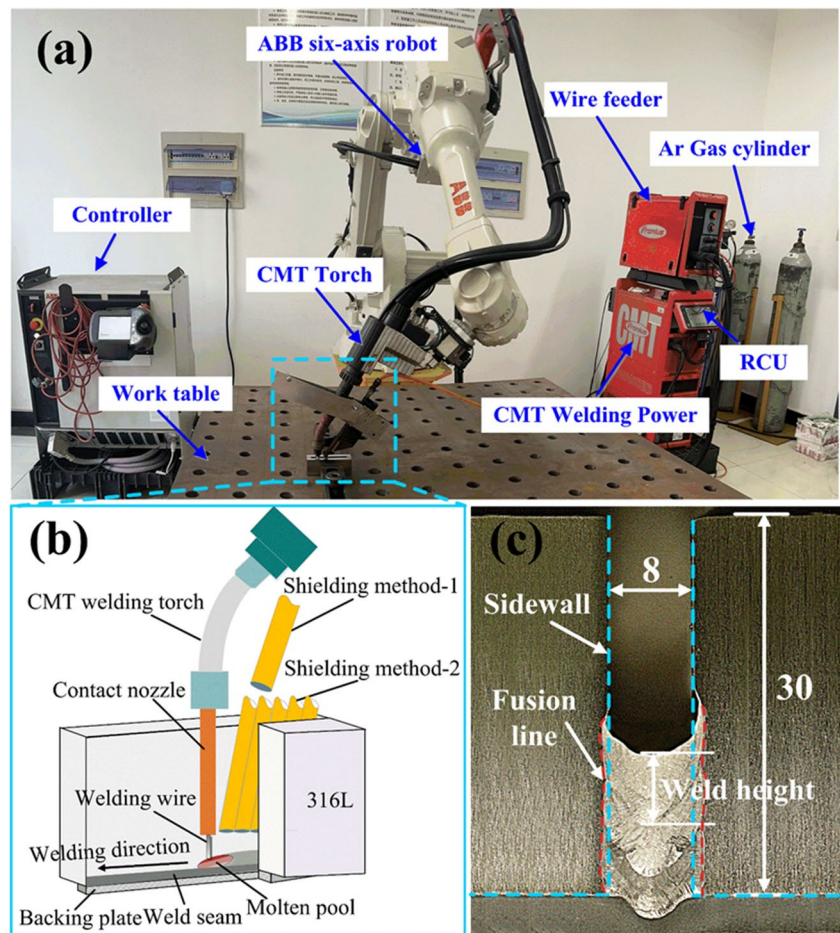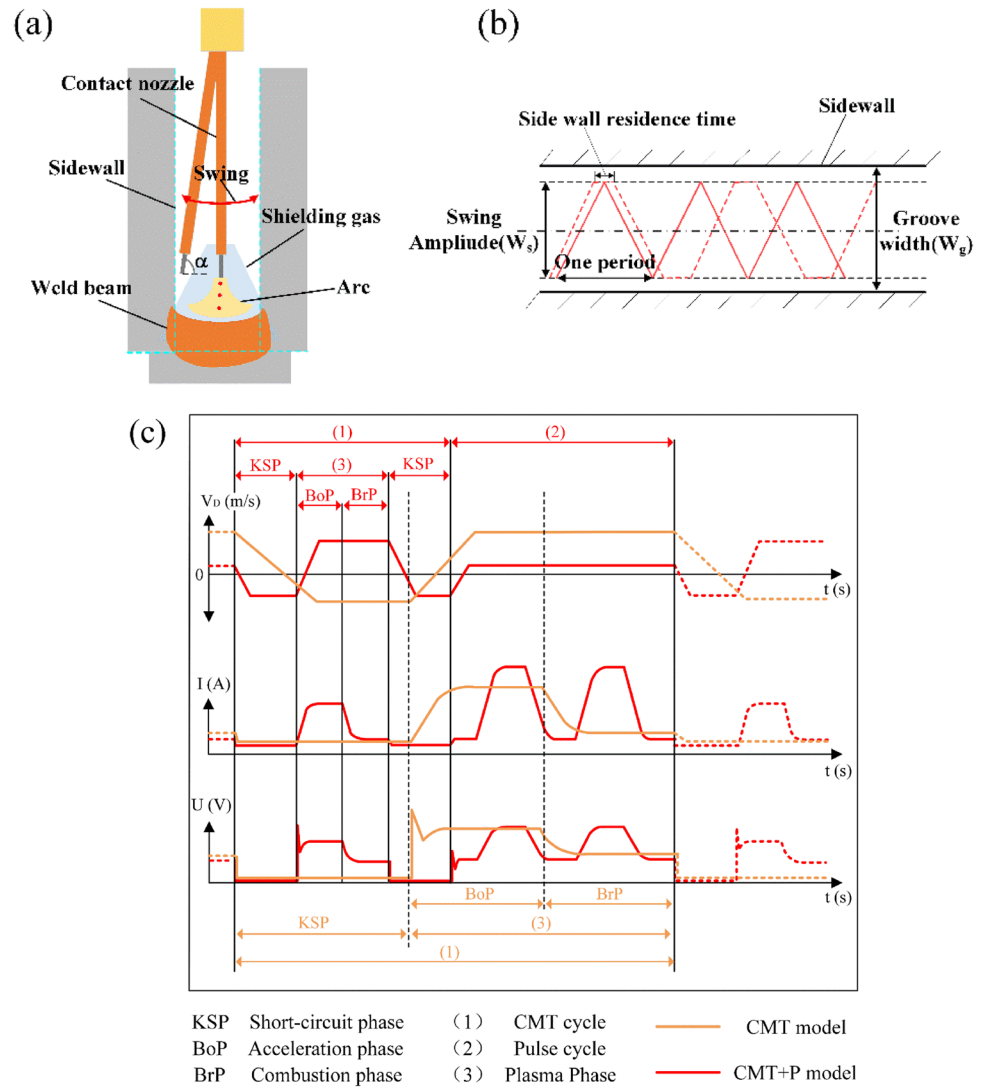

metal filling. In addition, due to the narrow and deep groove, the size requirements of the shielding gas nozzle and the conductive nozzle were higher. The effects of built-in and external nozzles on weld formation were studied experimentally. In order to adapt to the size of the groove and the arc swing space, it was appropriate to choose a 4-mm shielding gas copper tube as the built-in shielding gas nozzle. Moreover, according to the preliminary welding experiments, the selection of an 8-mm internal diameter gas nozzle had a better shielding effect on the molten pool, and could better adapt to the 8-mm groove gap. The two types of shielding gas nozzles indicated in Fig. 1b were employed. The drag shield for the built-in nozzle was made of a copper tube with an inner diameter of 4 mm (shielding gas-1). A copper tube with an inner diameter of 8 mm (shielding gas-2) was used to shield the external nozzle on the surface of the groove. The original conductive nozzle utilized in CMT welding was not suited for narrow gap welding. The experiments were carried out using self-made flat conductive nozzles with a thickness of about 2 mm and a length of 30 mm, which were sprayed with an insulating paint to prevent contact with the sidewalls. As presented in Fig. 1, before welding, the 316L steel plate was clamped with a fixture, the I-groove gap was

adjusted to 8 mm, and the 316L steel plate with a thickness of 10 mm was used as the substrate.

Weld shape was explored in terms of welding settings, swing, and protection strategies. The welding process had a wire extension of 15 mm, and the shielding gas formed a 60° angle with the welding torch and the robot arm swung at the predetermined speed and cycle, as shown in Fig. 1b. As shown in Fig. 2a and b, the robot is controlled by programming to swing the arc. The swing waveform is a triangular wave, and the main swing parameters include swing amplitude and swing frequency. When the welding current is too small or the welding speed is too large, the input heat is small, and the action time of the sidewall is too short, which easily leads to the lack of fusion of the sidewall. The welding current and welding speed selected for the experiment are 100–200 A and 2–6 mm/s. In addition, when the swing amplitude is too large, it will cause the arc to climb the wall, and when the swing amplitude is too small, the arc cannot fully contact the sidewall. When the swing frequency is too large, splashing is easy to occur in the welding process. Therefore, the swing frequency and swing amplitude are 0.2–8 Hz and 2–6 mm respectively. The welding process and swing parameters used in the experiment are

Fig. 2 Schematic of arc swing and pulse waveforms: **a** cross-section of arc swing, **b** arc swing waveform, **c** pulse waveforms for CMT + P and CMT welding processes

KSP	Short-circuit phase	(1)	CMT cycle		CMT model
BoP	Acceleration phase	(2)	Pulse cycle		
BrP	Combustion phase	(3)	Plasma Phase		CMT+P model

shown in Table 2. Figure 2c shows the pulse waveforms for CMT and CMT + P. In contrast to the CMT welding process, CMT + P was characterized by the addition of a number of pulse cycles after one or more consecutive CMT cycles. In CMT + P welding, the input heat can be controlled more accurately by the swing parameters in addition to the direct control of the current and voltage. As shown in Fig. 2, the

total pulse current of one cycle of CMT was greater than that of CMT + P, while the peak current of CMT + P was significantly higher. By optimizing the coupling effect of CMT + P pulse current and arc swing, it was beneficial to control the welding process stability and weld shaping.

Metallographic and tensile specimens were cut transversely along the welded joints by wire cutting, and electrolytic corrosion was carried out on the metallographic specimens after grinding and polishing, with an oxalic acid solution with a mass fraction of 10%, the power supply voltage set at 6 V, and the corrosion time set at 30 s. The macroscopic morphology and microstructure of the welded joints were examined using an optical microscope (Zeiss AXIO, Germany). The microstructure and tensile fracture morphology of the joints were examined using a scanning electron microscope (JSM-6510LV, Japan Electronics). The built-in OIM system was employed for the analysis of the electron backscattering technique (EBSD) to analyze the crystallographic characteristics of welded

Table 2 Narrow gap CMT welding process parameters

Welding parameters	Values
Welding current, A	100–200
Welding voltage, V	17.3–18.9
Welding speed, mm/s	2–6
Swinging amplitude, mm	0–6
Swing frequency, Hz	0.2–8
Welding torch angle, °	0–10
Shielding gas flow rate, L/min	Pure Ar, 15

joints. An HV-1000 microhardness machine was used to test the hardness with a load of 300 g and dwell times of 10 s at 0.2-mm intervals. The tensile test was carried out using a microcomputer-controlled electronic universal testing machine at a tensile speed of 2 mm/min. The position and size of the tensile specimen are shown in Fig. 3.
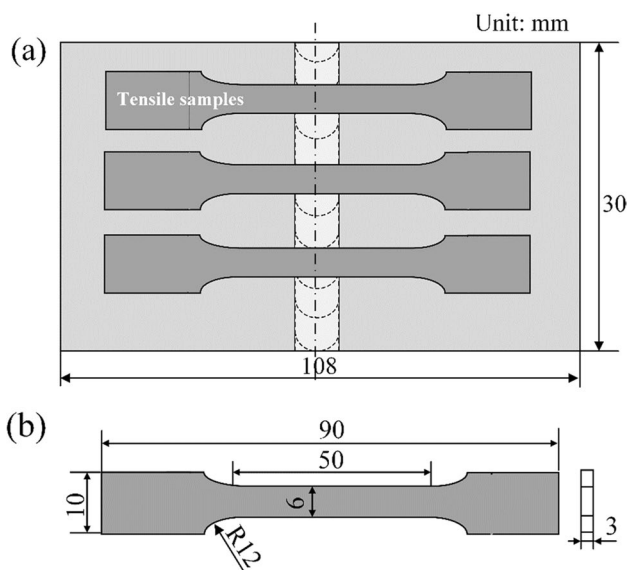
3 Results and discussion

3.1 Narrow gap weld geometry characteristics

Figure 4 illustrates the cross-sectional shape of the weld at various welding currents and speeds in the externally shielded mode. Due to the unified adjustment of the CMT welding process, the heat input and wire feeding speed increased with the increase of welding current. As shown in Fig. 4a, with the increase of welding current, the weld height and penetration increased, but the sidewall penetration did not increase significantly. At a welding current of 100 A, the heat input and filler metal were insufficient, resulting in the solidification of the sidewall and the weld toe without sufficient melting. Moreover, the sidewalls and weld toes were well fused at currents above 120 A, and the shape was concave semi-circular with no undercut. At welding speeds less than 4 mm/s, the weld shape changed from semi-elliptical to semi-circular, with improved fusion of the sidewalls and weld toes in Fig. 4b. The reduction in welding speed significantly increased the heat input and weld metal filler, but had no effect on sidewall penetration. When the welding speed exceeded 5 mm/s, the weld was asymmetrically distributed with unfused voids on one side of the groove. In the narrow

Fig. 3 Sampling position and size of tensile specimen: **a** sampling location, **b** specimen size

gap welding process, the metal in the fusion pool flowed rapidly from the front to the tail under the force of gravity. Although the arc and molten pool were more stable at a large welding speed, the welding heat input was reduced and the ability to melt the sidewall was weakened.

In CMT ultra-narrow gap unified welding, with the increase of welding current or the decrease of welding speed, the increase of welding heat input and weld metal filling amount is beneficial to the improvement of sidewall fusion [26]. Also, when the melting pool cooled faster or the filler metal was thicker, the influence of the welding arc on the bottom and sidewalls of the melting pool was lessened. The liquid metal at the bottom of the molten pool was difficult to fully diffuse under the action of surface tension, and the solidification rate was fast, which was prone to unfused defects. More liquid metal gathered below the arc with more filler metal in a single-pass weld, preventing the arc from heating directly to the bottom of the molten pool and, in particular, limiting the toe from obtaining sufficient energy to melt. Likewise, the welding arc expelled a large amount of liquid metal to the sides, and the arc could not directly heat the sidewalls, which were melted by heat conduction through the molten pool, resulting in a small depth of fusion. To avoid unfused defects on the weld toe and achieve a suitable sidewall depth of fusion, increasing the heat input and employing weld filler were insufficient.

The swing arc was crucial for controlling the stability of the weld pool in narrow gap welding by spreading arc energy, promoting heat dissipation, and increasing sidewall melting [27]. Consequently, the arc swing (frequency and amplitude) was used to control welding heat input and the dynamic behavior of the weld pool in order to optimize the welding formation. Figure 5a displays the cross-sectional shape of the weld at various swing amplitudes. When the swing amplitude was 0 mm, the interface between the weld passes was well fused, but the arc being farther from the sidewall caused a substantial lack of fusion on one sidewall and a reduced arc energy acting on the sidewall. As the swing amplitude increased, the arc approached the sidewall, more heat was transferred from the arc to the sidewall, and the sidewall penetration increased. When the swing amplitude was 6 mm, the molten pool was biased towards the side of the groove. On the other side, there was an undercut defect, and an unfused cavity was formed after welding the next one. Figure 5b presents the cross-sectional shape of a weld at various swing frequencies. As swing frequency increased, the weld metal deviated to one side of the groove, while the other side appeared to have unfused sidewalls. The sidewalls fused well when the frequency of swinging was small; however, the toe appeared slightly poorly fused. There was no significant difference in the depth of fusion and weld height of the sidewall at various swing frequencies. In addition, when the swing frequency was greater than 2 Hz, the

Fig. 4 Cross-sectional morphology of narrow gap weld with varying welding current and speed: **a** welding current, **b** welding speed
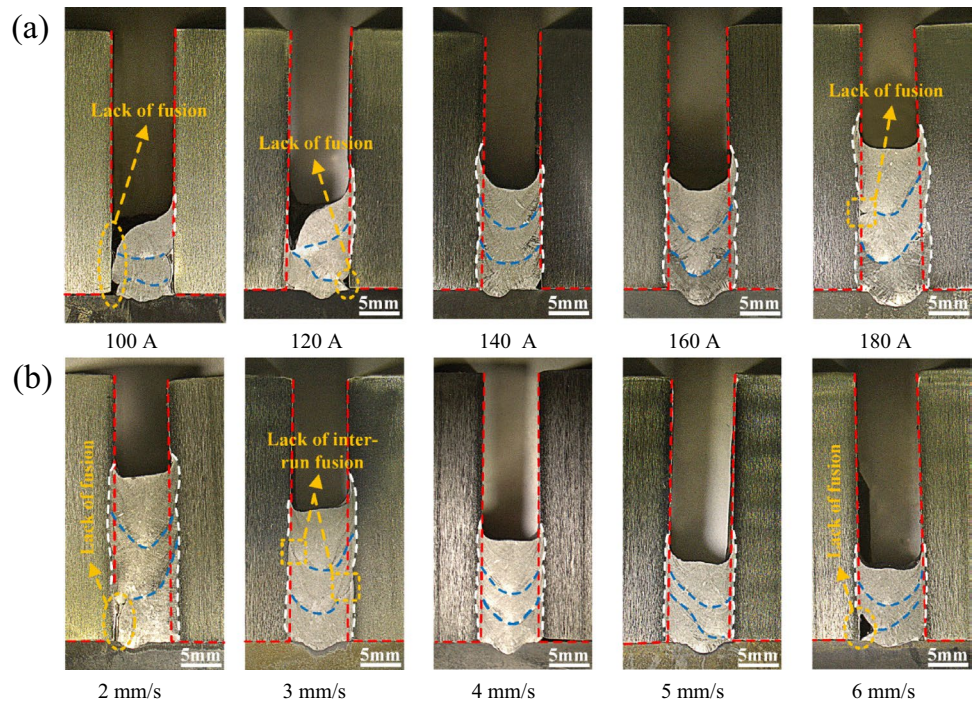

weld showed asymmetry and additionally poor fusion on one side of the groove.

Figure 6 shows a weld cross-section in the built-in shielding mode. Due to the small diameter of the built-in shielding gas tube, the limited shielding area, and the high blowing force, air easily entered the molten pool, resulting in large-sized air porosity. At welding speeds of 3 mm/s and 4 mm/s, large porosity was observed in the weld seam, as shown in Fig. 6a. At a welding speed of 6 mm/s, no significant porosity was found. In the narrow gap welding process, although the welding speed was low, the solidification time of the molten pool was long, which was beneficial to the

Fig. 5 Cross-sectional morphology of narrow gap welds with different swing width and swing period: **a** swing amplitude, **b** swing period
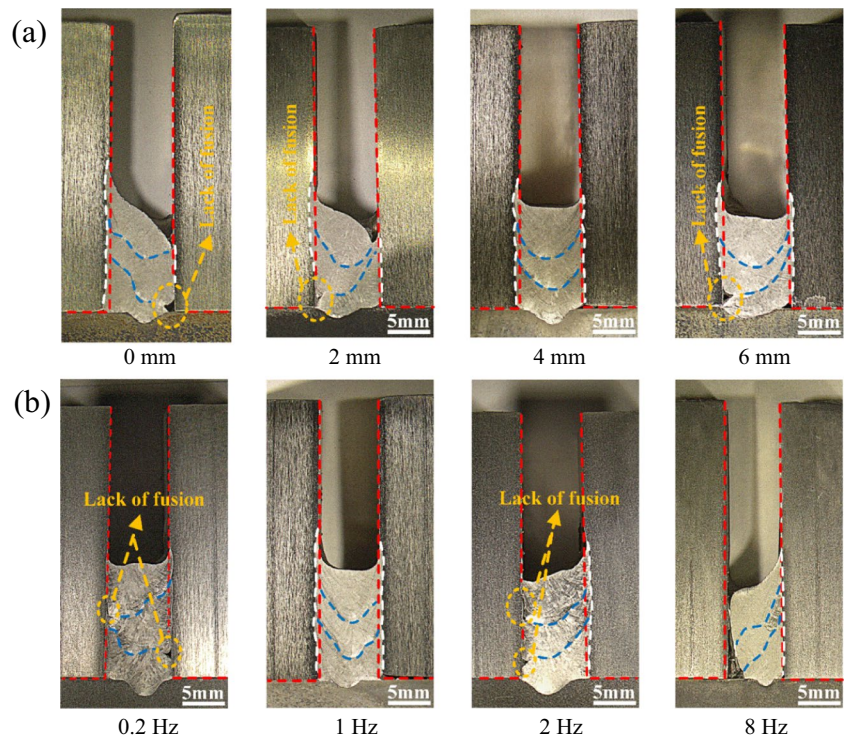
Fig. 6 Cross-sectional morphology of narrow gap welds using the built-in weld shielding method: **a** welding speed, **b** swing amplitude

(a)

| 2 mm/s | 3 mm/s | 4 mm/s | 5 mm/s | 6 mm/s |

(b)

| 0 mm | 2 mm | 4 mm | 6 mm |
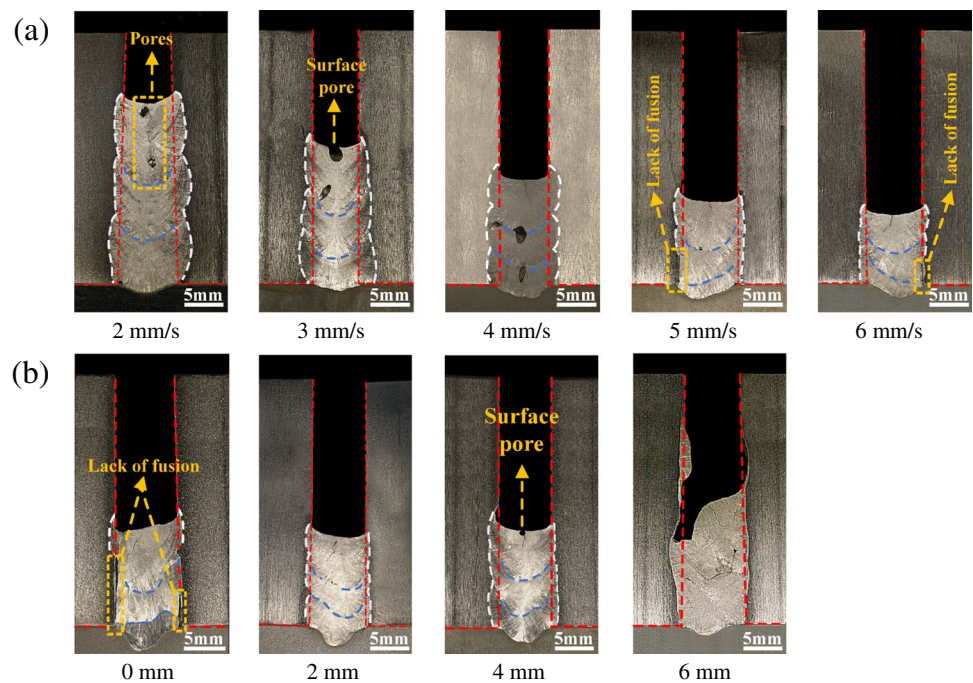
escape of bubbles in the molten pool. However, at low welding speed, the filling amount of weld metal was large, and the thickness of the molten pool was large, which was not conducive to the escape of bubbles. In addition, the side blowing gas had little effect on the molten pool at high welding speed, and the external air was not easy to be involved in the molten pool. Figure 6b shows the cross-section morphology of weld formation in various swing amplitudes. The weld shaping was similar to that of external protection, and the sidewall depth of fusion was larger than that of the external shield. Significant porosity appeared in the weld with a swing amplitude of 4 mm. The narrow gap welding process window of the built-in shielding method is small and the stability of the welding process is poor. Despite the fact that the weld was prone to porosity, the sidewalls were properly fused and the sidewall depth of fusion was greater than that of the external shielding approach. Nevertheless, the built-in shielding helped to keep the arc stiffness and the molten pool flowing.

The weld forming parameters were determined as the weld height (Hw) and the melting depth of the sidewalls (Hs) as a function of the weld geometry to assist the investigation of narrow gap weld shaping characteristics. Figure 7 shows the weld seam dimensions for various welding locations and swing parameters. As indicated in Fig. 7, increasing welding current and decreasing welding speed increased the sidewall depth of fusion, but swing width and frequency had little effect. The heat acting on the sidewall decreased as welding speed and increased as the current increased, resulting in an increase in the sidewall depth of fusion. The melt depth in the sidewall was 0.9 mm at a swing width of 4 mm.

The melt depth in the sidewall was 0.96 mm at a 1-Hz swing frequency. With smaller or larger swing widths, the sidewall melt depth did not increase significantly and the swing frequency had little effect. When the arc was close to the sidewall, the arc wall climbing phenomenon caused higher heat loss from the arc and a decrease in the sidewall depth of melt. The heat conduction from the molten pool to the sidewall became difficult as the swing frequency increased, making it challenging to melt the sidewall.

The melting sidewall depth is determined by the arc direct heating of the sidewall and heat conduction in the melt pool, whereas the swing angle, sidewall residence time, and their interactions have a greater impact on the melting sidewall heat. As the swing angle and sidewall dwell time increased, the continuous heating duration of the arc to the sidewall increased as did the amount of arc heat supplied to the sidewall, both of which helped in improving the sidewall melted depth. Figure 8 illustrates the morphology of weld shaping with various swing angles and sidewall dwell periods. As seen in Fig. 8, the weld morphology changed from a U-shape to a V-shape as the swing angle increased. Despite an insignificant increase in sidewall fusion depth, an unusable hole emerged in the weld toes. When the swing angle was large, the thermal effect of the arc on the sidewall increased, and the penetration depth on both sides of the groove increased. With the increase of the swing frequency, the filling metal and heat input increased, the molten pool stayed at a high temperature for a long time, and the sidewall penetration increased. However, the increase in weld thickness often led to poor fusion near the weld toe as shown in Fig. 8b.
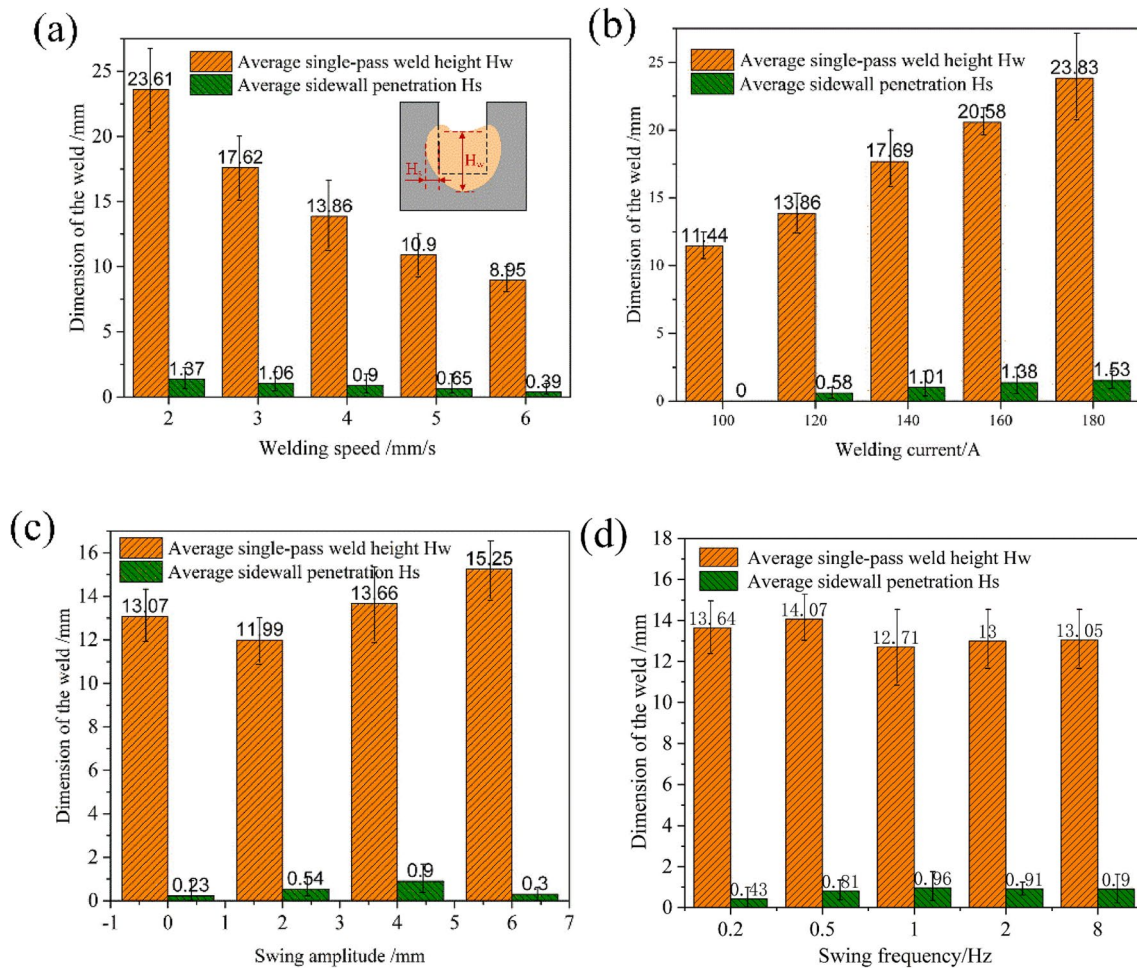
Fig. 7 Weld geometry with various welding parameters and swing parameters: **a** welding speed, **b** welding current, **c** swing amplitude, **d** swing cycle

According to the forming characteristics of narrow gap welds under different process parameters, the weld cross-section morphology is divided into symmetrical welds and asymmetric welds, and the weld defects are divided into poor sidewall fusion (Ls), insufficient weld toe fusion (Lt), and porosity defects. The arc pattern, melt pool flow, and droplet transition all had a significant impact on defect generation and weld morphology. Figure 9 exhibits a schematic diagram of weld shape and defect generation under various welding procedures. As shown in Fig. 9a, when the welding current was low, the welding arc energy and the amount of filling metal were insufficient, and it was difficult to melt the sidewall only by arc heating. Moreover, the cooling rate of the molten pool was slower under high heat input, and the molten metal could flow more easily to both sidewalls. As seen in Fig. 9b, when the welding current and swing amplitude were appropriate, the heat and mass between the sidewall and the molten pool metal could be well transferred under the combined action of the arc and the molten pool,

and the sidewall interface is well fused. When the arc swing is large, the arc is attracted by the sidewalls and deflected to one side of the groove sidewalls, while the other side of the groove sidewalls is not sufficiently heated, as shown in Fig. 9c. The direction of plasma flowing force and electromagnetic force on the droplet was diverted when the arc was deflected to the sidewall side, and the current line pointed from the droplet to the sidewall. The molten metal accumulating on one side of the slope caused the weld asymmetry on both sides of the slope. A sloping weld was eventually developed, resulting in a lack of fusion on the sidewall side. Thus, when the welding heat input and swing were appropriate, the arc burnt persistently and the groove bottom and sidewalls were properly heated and fused in synchronization.

Figure 10 presents a schematic illustration of the creation process of unfused defects in the weld toes under high heat input. As shown in Fig. 10a, the high-temperature residence time increased at high heat input and the effect of the arc on the sidewall increased. More arc and pool heat was delivered
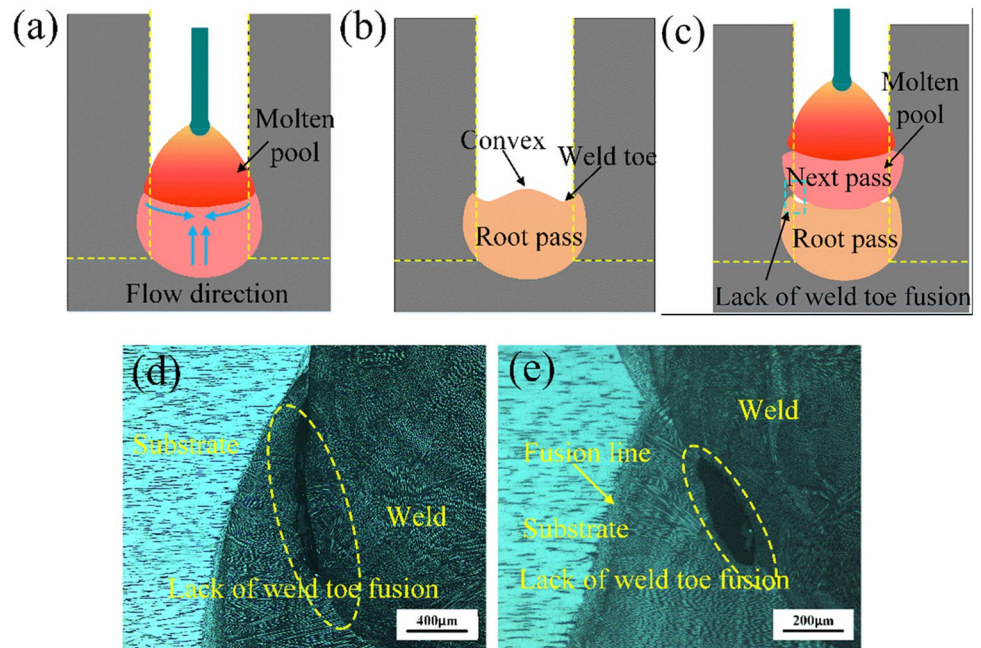
Fig. 8 Cross-sectional morphology of weld with different swing angles and sidewall dwell times: **a** swing angle, **b** sidewall dwell time
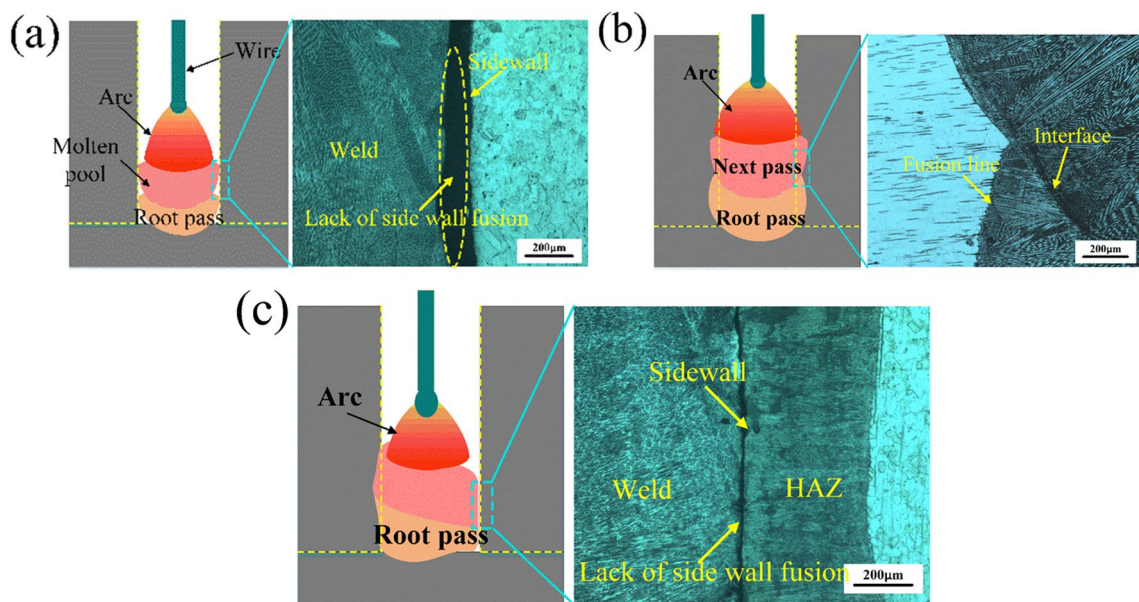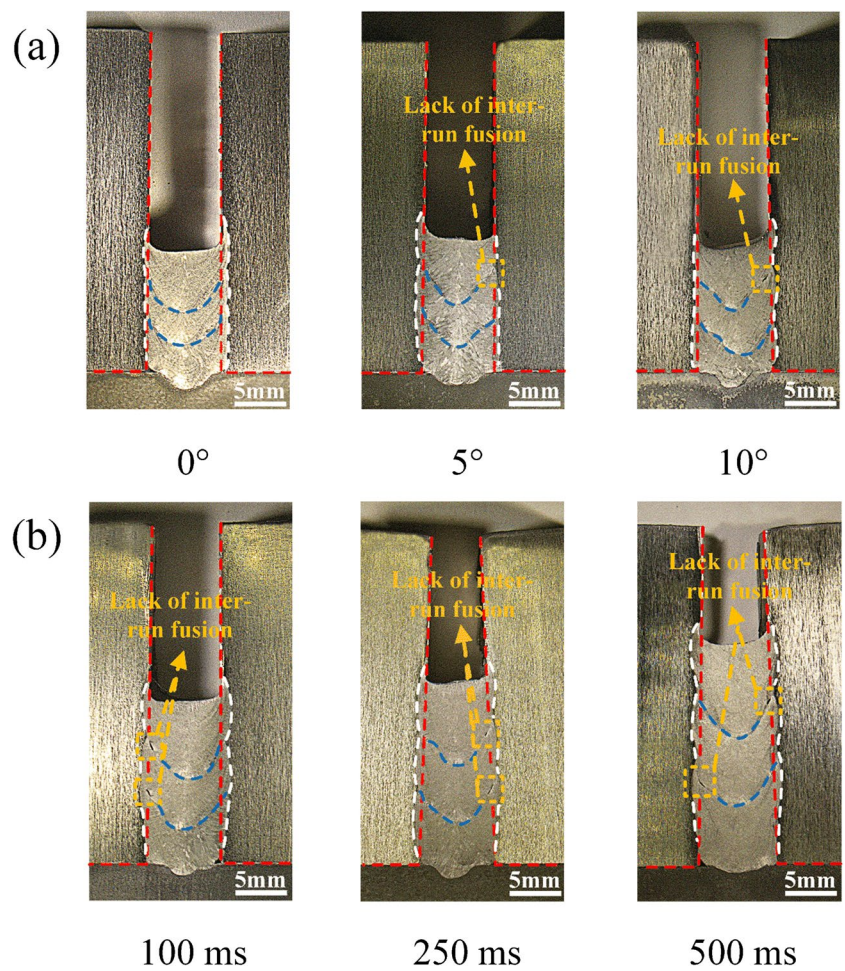
Fig. 9 Mechanism of formation of unfused defects in narrow gap welds

Fig. 10 Mechanism of formation of unfused defects in the weld toes

to the sidewall and weld toe location when filling the initial weld, and the sidewall was well fused. In addition, the molten metal at the weld toe entered the weld pool under the action of gravity, forming an obvious undercut (the weld toe was concave into the sidewall), as shown in Fig. 10b. Due to the enormous amount of filler metal used in the second weld, the arc heat could not be transferred to the toes, making it impossible for the molten metal to fill the toe and nibble the edge under the action of surface tension, resulting in an obvious infused weld toes.

Figure 11 shows the cross-sectional morphology of narrow gap weld with different wire feed speeds. As demonstrated in Fig. 11, increasing the amount of weld metal filler (wire feed speed) in a single pass resulted in a significant increase in weld height. When the wire feeding speed was 140 A, 9 welding passes could fill the groove, but when the wire feeding speed was 200 A, only 4 passes were needed

to fill the groove. Besides, increasing the amount of filler metal for a single pass did not significantly increase the sidewall fusion depth, but rather caused it to fluctuate, especially when the amount of filler metal was too large, the single-pass weld produced a significant undercut, resulting in an obvious poor fusion, as shown in Fig. 10c.

3.2 Microstructure

Austenitic stainless steel welds can be classified into four types based on their cooling process solidification and solid-state phase transition mode: full austenite (A), austenite-ferrite (AF), ferrite–austenite (FA), and full ferrite (F). Austenite and ferrite morphology varies with solidification mode, with ferrite morphologies including eutectic, cytosolic, skeletal, lath, spherical, and wormlike [28]. Figure 12 shows the macroscopic and microscopic metallography of

Fig. 11 Weld shaping and defect morphology for different weld filler amounts: **a** 140 A, **b** 180 A, **c** 200 A
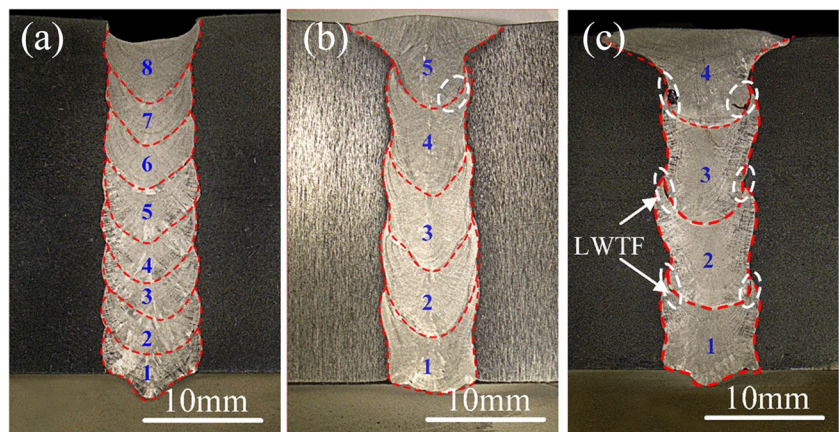
Fig. 12 Macro- and micro-structure of narrow gap welded joints under low heat input: **a–d** bottom, **e–h** middle, **i–l** top
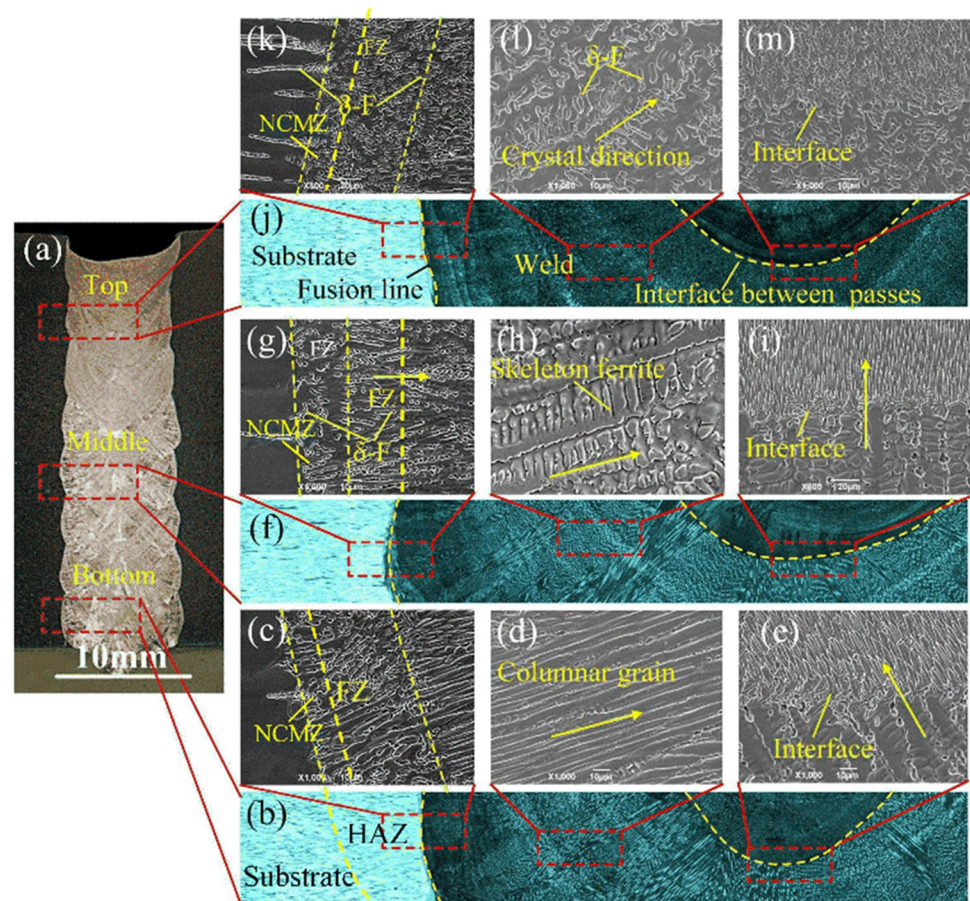
narrow gap welds. Figure 12a illustrates the observation position of micro-morphology in the welded joints. The metallographic examination of the lower part of the weld is depicted in Fig. 12b–e. As illustrated in Fig. 12b, the cross-section of the low heat input welded joint was divided into five regions: base metal (BM), heat-affected zone (HAZ), fusion zone (FZ), weld (side and middle). The macroscopic morphology of the weld revealed apparent layering characteristics, which were primarily produced by changes in the microstructural morphology caused by the distinct temperature gradients. The microstructures of the base metal and HAZ did not differ appreciably, and both were composed of austenite and some amount of striated δ-ferrite. The non-convective mixing zone (NCMZ) refers to the region near the fusion line in which the base metal undergoes melting but does not thoroughly mix with the filler material. Essentially, it is the boundary area of the molten pool that experiences limited convective mixing and is primarily subject to diffusive blending. After solidification, this area forms an uneven region with a predominant composition derived from the base metal. The non-convective mixing zone (NCMZ) near the fusion line is about 60 μm wide, the ferrite is spherical and lath-like, and the weld grain shows epitaxial growth characteristics [29]. The weld displayed predominantly

typical columnar crystallites with a width of 5 µm, as shown in Fig. 12d, generated by quick cooling of the bottom part of the weld. The fusion interface was visible in the middle of the weld, and grain development was parallel to the fusion line, but the morphology was substantially different, as seen in Fig. 12e. There are some small approximately equiaxed austenite grains above the weld fusion lines and some larger austenite grains below the fusion lines, whose orientations are relatively dispersed. As shown in Fig. 12e and i, the size of the ferrite above the fusion lines is smaller than that below the fusion lines, but the content of the ferrite on both sides of the weld is similar.

Figure 12f–i show the macroscopic and microscopic morphology in the middle of the weld. Figure 12g illustrates the microstructure near the fusing line. As shown in Fig. 12g, the width of NCMZ was approximately 30 µm, and the ferrite shape was predominantly spherical and wormlike. The weld was mostly made up of columnar dendrites with visible secondary dendrites, and the ferrite morphology was skeletal. The microstructure of the center of the weld was composed of coarse dendritic crystallites, but no primary dendrites are seen in Fig. 12h and i. Figure 12j–m show microstructure of the upper part of the weld. As shown in Fig. 12k, the fusion line and NCMZ were not evident and

more ferrite was retained. Microstructure of weld was dominated by coarse dendrites which were interconnected and showed a reticulated structure, consisting of initial ferrite dendrites and austenite between the dendrites, and the direction of grain boundaries and grain growth was not obvious. The grain growth in the middle of weld was not significant, and there was a tendency to transform into an equiaxial crystal, as shown in Fig. 12m.

The relationship between austenitic stainless steel weld crystallization morphology and temperature gradient is depicted in Fig. 13a. The temperature gradient G in the liquid phase at the solid/liquid interface during weld pool solidification and the growth rate V at the solidification front determine the morphology and size of the grains as well as the internal substructure [30]. As illustrated in Fig. 13, the lower the G/V, the easier it is to construct an equiaxial crystal structure, and conversely for a columnar crystal structure. The temperature gradient and growth rate inside the weld pool are not the same at different locations. Usually, the temperature gradient at the bottom of the melt pool is large, and the growth rate is small, which makes it easy to form columnar crystals. The temperature gradient at the top of the molten pool is small, and the growth rate is large, which makes it easy to form equiaxial crystals.

In narrow gap welding, single-pass layer-by-layer deposition is used to fill the groove, and the surface of the previous weld will be remelted (remelted zone). There is usually no equiaxed crystal in the remelting zone, while the columnar crystal at the bottom of the molten pool extends upward by epitaxial growth. The area below the fusion line between the two layers is affected by the heat of the next weld (weld heat-affected zone), and the microstructure shows a clear gradient. As can be seen in Fig. 12 and Fig. 13b, there are significant differences in grain morphology and size within each weld, and the phenomenon of "layering" occurs internally. The remelted zone is directly fused with the metal of the next weld, and the cooling rate is the fastest due to heat transfer, so it consists of fine columnar crystals (dashed ellipse), and the central zone consists of dendrites and cellular crystals (dashed circle). The growth direction of the grains in each region of each weld is basically the same, mainly along the longitudinal direction, which is due to the narrow gap welding process because the axial direction of the arc is along the longitudinal direction, so the longitudinal direction is the direction of the temperature gradient, which is the largest, but also the most conducive to the growth of the grains in the direction. In addition, the narrow gap welding molten pool has an extremely fast cooling rate during

Fig. 13 **a** Temperature gradient and growth rate as a function of micro-solidified crystalline morphology and size [34]. **b** Grain growth morphology in different weld regions under low heat input
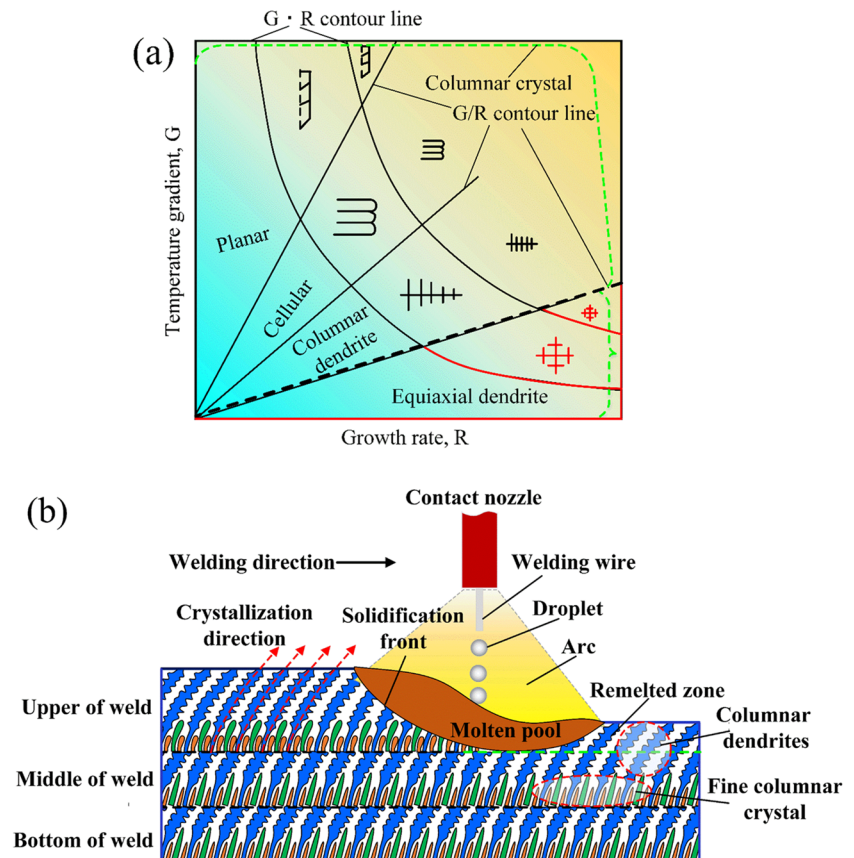
solidification, which limits the formation and growth of secondary dendrites.

The macro- and micro-morphology of narrow gap welds under high heat input is shown in Fig. 14. Despite the fact that the filler metal of the single-pass weld was greater under high heat input, the molten pool had a long residence time at high temperature, the temperature gradient was small, and the single-pass weld showed no noticeable delamination occurrence. Figure 14b–e indicate the macroscopic and microscopic morphology of the lower part of the weld. As shown in Fig. 14b and c, the fusion lines and grain boundaries were not visible, the weld exhibited associative crystallization properties, and the δ-ferrite was wormlike. As indicated in Fig. 14d, the weld microstructure was primarily columnar grain, the remaining high-temperature ferrite was less, and the width of the columnar crystals was much more than the low heat input. The crystal morphology of the central region of the weld was columnar dendrites, which grew perpendicular to the surface of the weld, and the dendrite spacing was larger, while the remelting zone was short columnar austenite grains. The microstructure of the central region of the weld is shown in Fig. 14f–i. As shown in Fig. 14f and g, the width of the partially melted zone is about 50 μm. Austenitic stainless steel has a small crystallization

temperature range and grows towards the weld center in the form of dendrites. Consequently, the microstructure of the welds on both sides shows coarse dendritic crystals, but the secondary dendrites are not significant. The equiaxed crystal is the main feature of the weld center area. Figure 14j–m show the microstructure of the upper part of the welded joint. The weld was mostly made up of coarse dendritic crystals, while the cellular crystals were barely visible. The dendrites in the center of the weld were exactly aligned along the base metal thickness direction.

As shown in Figs. 14j and 15a, significant longitudinal cracks were found in the upper part of the welded joints, mainly in the central region of the weld. The cracks extended and expanded along the subgranular boundaries of the dendrites in different orientations. The center of the weld presented solidified subgrain boundaries that displayed small-angle grain boundaries in crystallography in Fig. 14j. During solidification, the grains of weld metal crystallized along the preferred crystallization direction or easy growth direction, resulting in noticeable variances in solidification crystallization orientation. Crystalline cracks were easily formed and propagated along the solidified subgrain boundaries due to the micro-segregation of elements. Figure 15b shows the EDS surface scan of the cracked surface. Although there was

Fig. 14 Macro- and microstructure of narrow gap weld at high heat input: **a–d** bottom, **e–h** middle, **i–l** top
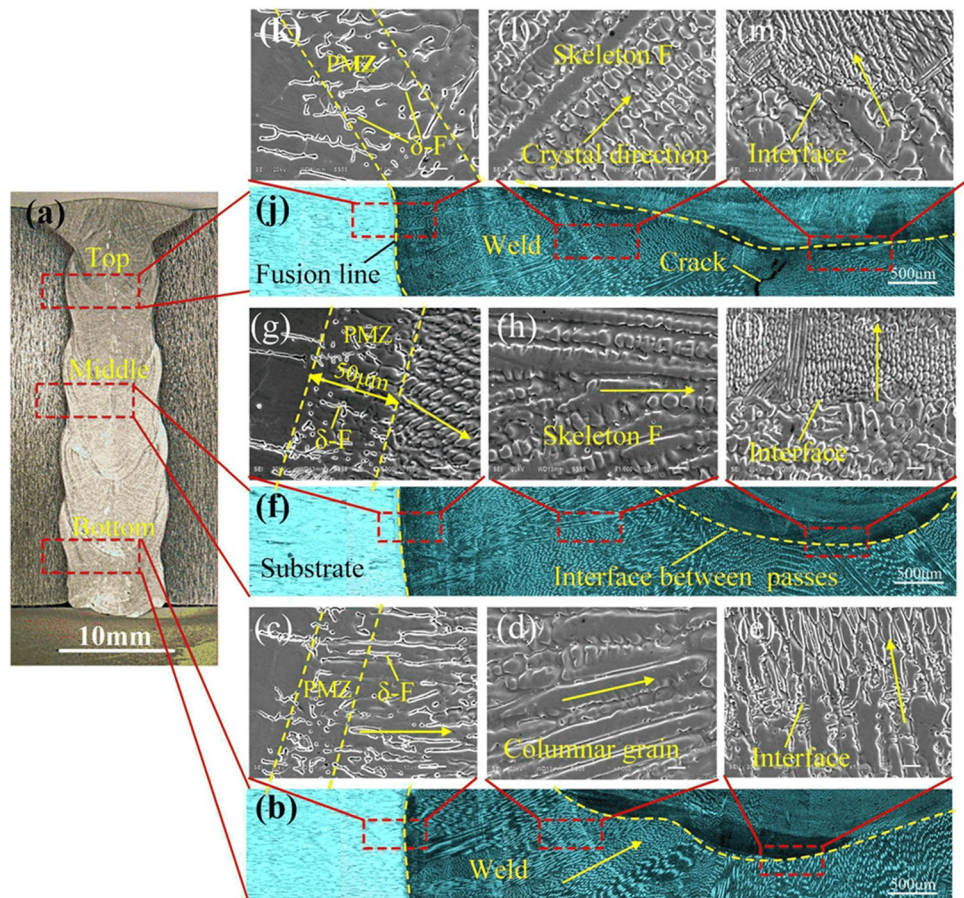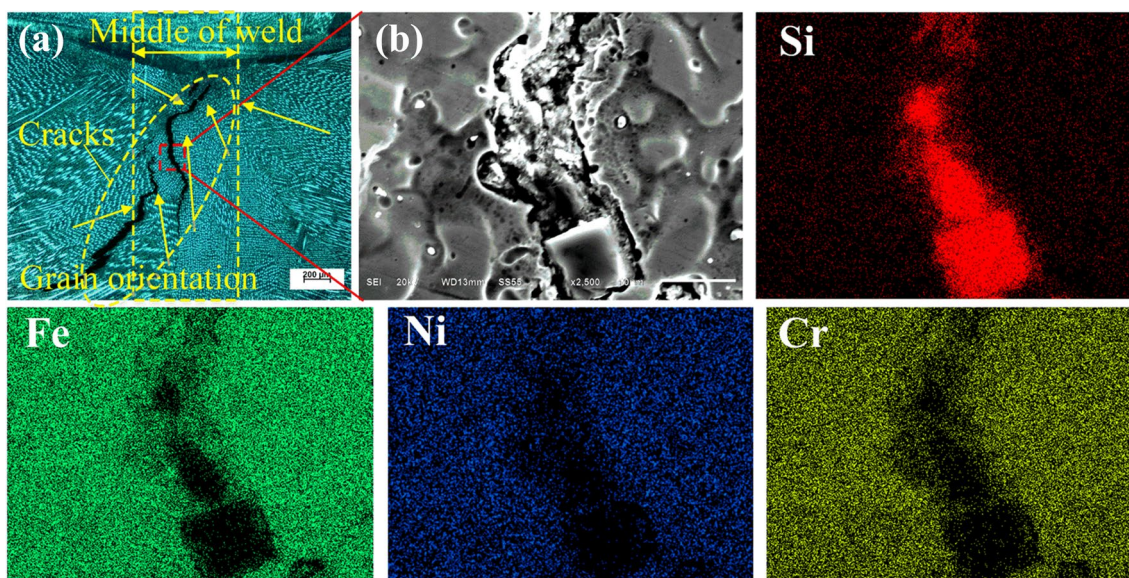
Fig. 15 Characteristics of weld solidification cracks under high heat input and EDS surface scan of cracked surface

no noticeable segregation of Fe, Ni, or Cr elements on the broken surface, the segregation of Si elements was visible. The low melting point eutectic elements of Si were polarized at the interface of grains with different orientations in the center of the weld, forming a low melting point eutectic liquid film during solidification and causing along-crystal cracking under the influence of shrinkage tensile stress.

The weld grain boundary (SGB) of austenitic stainless steel is formed by the competitive growth of grains along the edge of the molten pool during the solidification process, and the grain boundary always has a large angular orientation deviation [31]. Most of the subgrain boundary (SSGB) structure is an interface composed of cellular crystals, dendritic crystals, or equiaxed crystals in the weld center. It should be noted that it is difficult to identify SGB and SSGB only from the metallography of Fig. 13 and Fig. 14, and the grain morphology in HAZ is also difficult to observe. EBSD analysis was performed to further explore the grain growth characteristics. The orientation image maps of the base metal, HAZ, and weld metal are presented in Fig. 16. HAZ is composed of fine grains that exhibit the random orientation color distribution, with an average grain size of roughly 100 μm. Obvious columnar dendrites were produced both in the regions of weld metal, which grew in the direction opposite to the heat transfer direction. Under low heat input, the grains on both sides of the weld grow perpendicular to the fusion line, while short columnar crystals and a small amount of equiaxed crystals are formed in the center of the weld. Figure 16b and e display the KAM results for the weld, HAZ, and fusion zone. From Fig. 6b and e, it could be observed that the grain misorientation angle was primarily distributed in the interval of 0–5°, and that in different regions of the welded joint was not much different. The KAM under high heat input was slightly larger than that under low heat input. While the stress at the weld edge was higher than that in the middle of the weld, the HAZ stress was higher than that in the fusion zone. Between the HAZ grain boundaries and the columnar dendritic grain boundaries, the weld generated reticular stress distribution and linear stress distribution, respectively. The weaving of the weld was more apparent than the fusion zone and the HAZ. The pole figure (Pf) in Fig. 16c and f shows an apparent texture of {100}, and that both {110} and {111} presented symmetrical morphology. The crystallographic texture index was 4.501 n, and the maximum texture index was 8.969 near the weld center, much higher than that near the fusion line. The high texture index indicates a high texture trend and strong anisotropic microstructures.

The grains grew more preferentially along the direction perpendicular to the melt pool boundary, or< 100 >, which is the direction in which face-centered cubic crystals of austenitic stainless steels tend to grow [27]. In the narrow gap welding process, the weld crystal preferentially grows along the direction with the largest thermal gradient, and generally grows perpendicular to the sidewall fusion interface to the weld center. The distribution of the grain size was also calculated, and the results are shown in Fig. 16h and g based on the EBSD results. Because the heat-affected zone had small grains and the fusion zone had large grains, the dispersion of grain size near the fusion zone increased with increasing grain size. More than 60% of the grains had a diameter of less than 100 μm and were mostly found in the heat-affected zone. The weld grain size was substantially greater than in
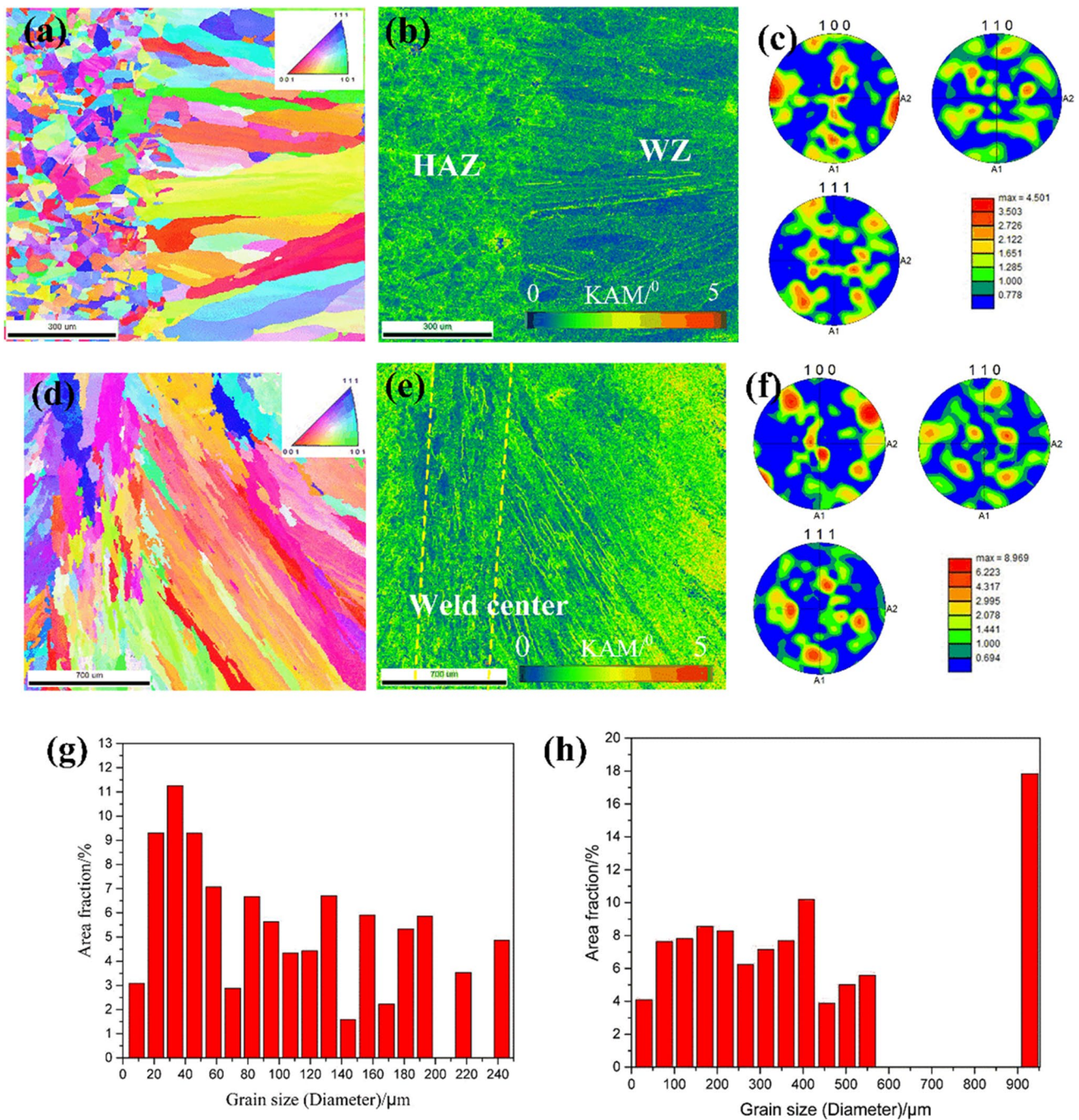
Fig. 16 EBSD analysis results of weld joint with low heat input. **a**, **d** Inverse pole figure (IPF); **b**, **e** KAM map; **c**, **f** IPF map; **h**, **g** grain size distribution of HAZ and WZ

the HAZ and fusion zone, with around 80% of the grains being 100–550 μm.

Figure 17 shows the crystallization of a narrow gap weld under various heat inputs. At low heat input, the microstructure of the weld is dominated by columnar dendrites perpendicular to the fusion line and underdeveloped secondary dendrites. The center of the weld is dominated by short columnar dendrites parallel to the fusion line. Under high heat input, the weld is dominated by columnar dendritic crystals with obvious coarsening characteristics, and the secondary dendritic crystals are well-developed, and the ferrite is in the form of a network or skeleton. The melt pool boundary temperature gradient (G) decreased as welding heat input increased, as did the G/R and $G \cdot R$ values. In the process of solidification and crystallization of the molten pool, the increase of composition undercooling is helpful

Fig. 17 Characteristics of crystallization morphology and formation mechanism of narrow gap welding process of austenitic stainless steel: **a** crystallization process of weld at low heat input, **b** crystallization process of weld at high heat input
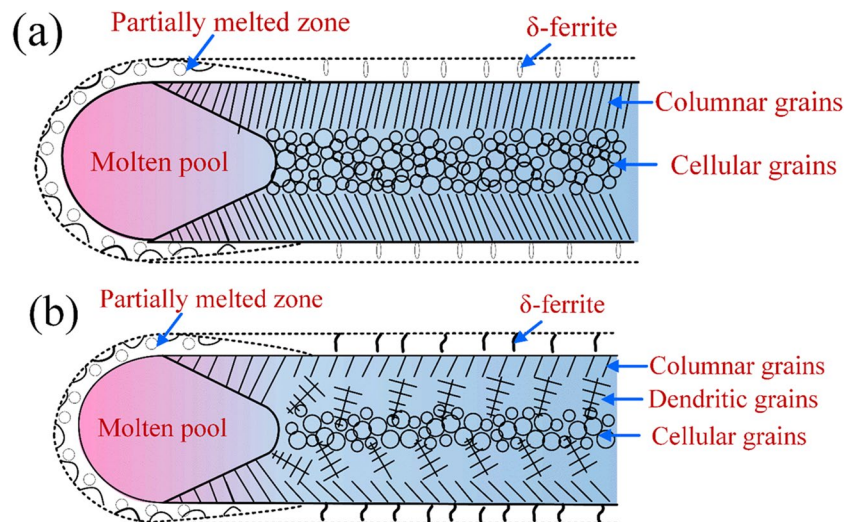

to form equiaxed grains, but the grains are easy to coarsen. Nonetheless, CMT narrow gap welding is a rapid heating and cooling process with a large degree of subcooling, which inhibits the nucleation and development of equiaxed crystals. However, in the middle and upper part of the high heat input weld, the high-temperature residence time is long and the temperature gradient is not obvious under the effect of heat accumulation [32]. Some equiaxed grains are formed adjacent to the columnar dendrites on both sides of the weld, as shown in Fig. 14h and l. In addition, the chemical inhomogeneity of 316L stainless steel welds is mainly characterized by micro-segregation and regional segregation. Microscopic segregation occurred mostly at the weld columnar dendritic grain border, while regional segregation happened primarily in the middle of the weld where dendritic clusters converged at the solidification subgrain boundary.

3.3 The mechanical properties of welded joints

Figure 18 shows the microhardness distribution of welded joints in various heat inputs. The microhardness of the welded joint was higher than that of the base metal at low heat input, as shown in Fig. 18a, with a difference of around 60 HV between the highest and minimum values. The microhardness at the bottom of the weld was higher than that at the top. Microhardness values in the weld metal varied significantly due to changes in the form and composition of austenite grains and ferrite. The grain size had a large influence on microhardness, according to Hall Petch's formula
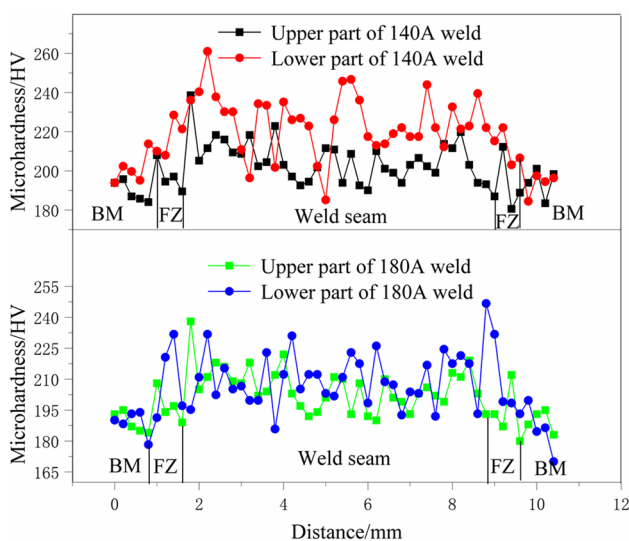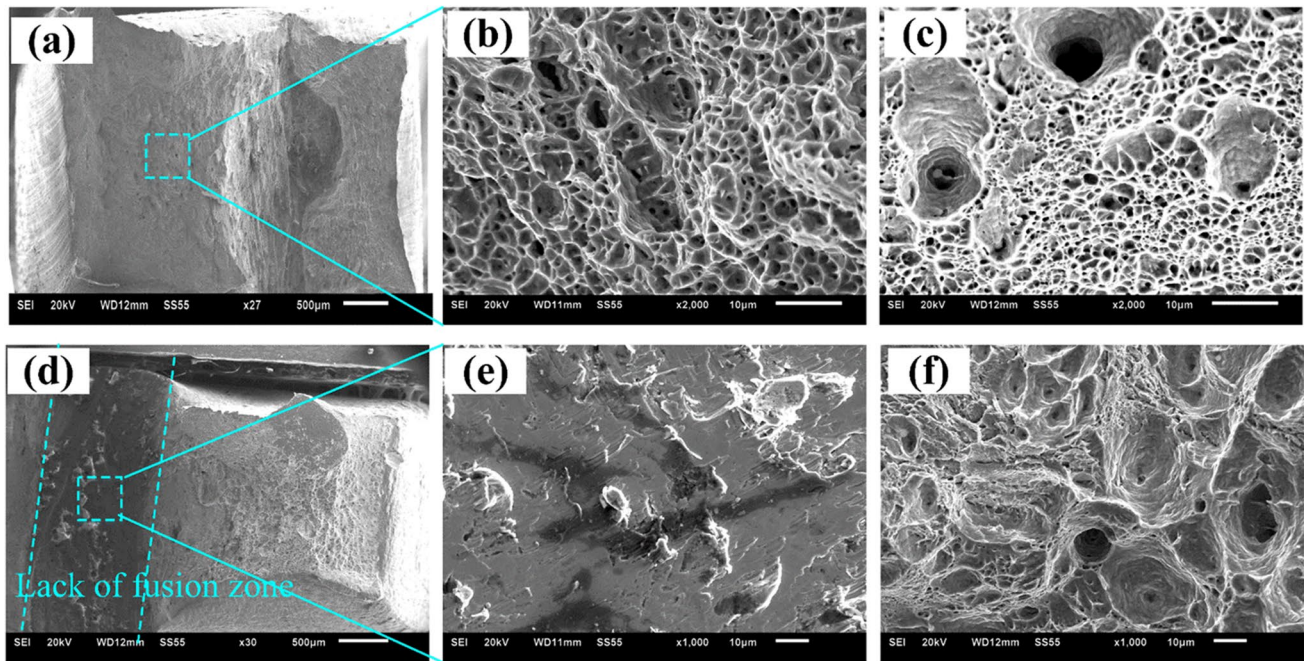

Fig. 18 Distribution of weld microhardness at different heat inputs. **a** 140 A, **b** 180 A
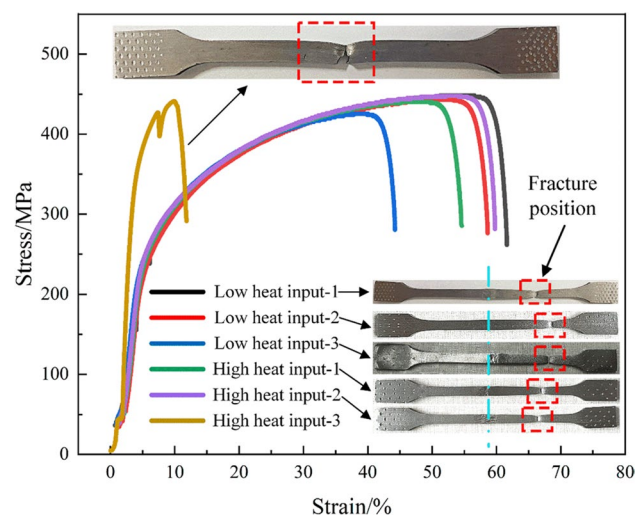
Fig. 19 Tensile stress–strain curve and tensile fracture location of narrow gap welded joints

Fig. 20 Fracture surface morphology of tensile specimen: **a–c** 140 A, **d–f** 180 A

[33], since grain boundaries are effective potential barriers for dislocation motion. The microhardness of the high heat input weld was slightly lower than that of the low heat input weld, owing to coarser columnar grains and more ferrite production, and the distribution pattern of the weld, heat-affected zone, and base metal was similar to that of the low heat input, with the weld hardness value remaining higher than the base metal.

Experimental research was done on the tensile characteristics of welded connections at various locations and under various heat inputs. The stress–strain curves and tensile fracture locations of narrow gap welded joints are depicted in Fig. 19. As shown in Fig. 19, the average tensile strengths of the low and high heat input welded joints were 430 MPa and 420 MPa, respectively. Defect-free tensile specimens with low heat input were all fractured in the base material away from the weld (middle position), and there was obvious necking at the fracture position, obtaining a welded joint with excellent static mechanical properties. Additionally, when unfused defects were present in the welded joint, the specimens tended to fracture at the defects. For instance, the high heat input specimen-3 tensile stress–strain curve (dashed line) broke close to the fusion line. The tension fracture morphology of welded joints is shown in Fig. 20. The low heat input tensile specimen's fracture surface was composed of tiny equiaxial dimples, as shown in Fig. 20a–c, and the fracture displayed typical ductile features. As seen in Fig. 20c, there was a significant variation in the size of dimples on the fracture surface, which was explained by the

existence of coarse cellular crystals and elemental segregation inside the dendritic grains. Figure 20d and e show the fracture surface morphology of tensile specimens of welded joints with unfused defects at high heat input. The dark area was the unfused position with a flat fracture surface, while the other areas were dominated by dimples. Moreover, due to the coarse grain size of the high heat input weld and the presence of δ-ferrite at the grain boundaries, the fracture morphology exhibited large-size dimples and tear ribs with quasi-cleavage features.

4 Conclusions

In this work, the forming characteristics, microstructure, and mechanical properties of 316L manufactured by NG-CMT welding were studied. The conclusions can be summarized as follows.

(1) The 30-mm-thick 316L austenite stainless steel plate and a groove gap of 8 mm were successfully welded by NG-CMT swing welding, and were free of pores or cracks, as well as exhibited no lack of fusion with low heat input. Arc swing and shielding mode had a substantial impact on the fusion behavior of the sidewalls and toes in narrow gap welding.

(2) The microstructure was mainly composed of austenite and a small amount of ferrite, and the heat-affected zone was fine-twinned austenite. The dendritic solidi-

fication subgrain boundaries in the middle of the weld under high heat input led to the formation of longitudinal solidification cracks.

(3) The columnar grains of the weld metal predominated in < 100 > orientation, but the twin crystals of HAZ mainly grew in different orientations. The insufficient phase transition from the δ-ferrite to the γ-austenite resulted in a larger amount of residual intergranular δ-ferrite in the FZ.

(4) The microhardness of the weld was higher than that of base metal and HAZ. The average tensile strength of the weld joint was 430 MPa, which was equivalent to the base metal. The tensile strength of welded joints was comparable to that of the base material. This was experimentally corroborated by the fact that the fracture surface was composed of tear ridges and fine equiaxed dimples.

Data Availability Not applicable.

Code availability Not applicable.

Declarations

Ethics approval Not applicable.

Consent to participate Not applicable.

Consent for publication Not applicable.

Conflict of interest The authors declare no competing interests.

References

1. Anant R, Ghosh PK (2017) Ultra-narrow gap welding of thick section of austenitic stainless steel to HSLA steel. Journal of Materials Processing Tech 239:210–221. https://doi.org/10.1016/j.jmatprotec.2016.08.016

2. Yang WX, Xin JJ, Fang C, Dai WH, Wei J, Wu JF, Song YT (2019) Microstructure and mechanical properties of ultra-narrow gap laser weld joint of 100 mm-thick SUS304 steel plates. J Mater Process Tech 265:130–137. https://doi.org/10.1016/j.jmatprotec.2018.10.017

3. Buddu RK, Chauhan NL, Raole PM (2014) Investigations of microstructure and mechanical properties of 60-mm-thick type 316 L stainless steel welded plates by multipass tungsten inert gas welding and electron beam welding for fusion reactor applications. Fusion Sci Technol 65:248–254

4. Anant R, Ghosh PK (2017) Ultra-narrow gap welding of thick section of austenitic stainless steel to HSLA steel. J Mater Process Technol 239:210–221. https://doi.org/10.1016/j.jmatprotec.2016.08.016

5. Elmesalamy A, Francis J, Li L (2014) A comparison of residual stresses in multi pass narrow gap laser welds and gas-tungsten arc welds in AISI 316L stainless steel. Int Press Vessel Pip 113:49–59. https://doi.org/10.1016/j.ijpvp.2013.11.002

6. Dittrich D, Schedewy R, Brenner B (2013) Laser-multi-pass-narrow-gap welding of hot crack sensitive thick aluminum plates. Phys Procedia 41:225–233. https://doi.org/10.1016/j.phpro.2013.03.073

7. Wei B, Jia CB, Wu W, Fang C, Wu CS (2020) Stirring effect of the rotating arc on the molten pool during non-axisymmetric tungsten NG-GTAW. J Mater Process Technol 285:116769. https://doi.org/10.1016/j.jmatprotec.2020.116769

8. Rai R, Palmer TA, Elmer JW, Debroy T (2009) Heat transfer and fluid flow during keyhole mode laser welding of tantalum, Ti–6Al–4V, 304L stainless steel and vanadium. J Phys D Appl Phys 40(18):5753. https://doi.org/10.1088/0022-3727/40/18/037

9. Wang MQ, Wu PB, Xu K, Huang RS, Wang XX, Fang NW, Sun LB, Qin J, Ma YM, Su JH (2023) Influence of high-temperature annealing on microstructure and properties of welded joints using narrow gap laser welding of TC4 titanium with welding wire. J Mater Eng Perform. https://doi.org/10.1007/s11665-023-08629-3

10. Cai XY, Lin SB, Fan CL, Yang CL, Zhang W, Wang YW (2016) Molten pool behaviour and weld forming mechanism of tandem narrow gap vertical GMAW. Sci Technol Weld Joining 21(2):124–130. https://doi.org/10.1179/1362171815Y.0000000073

11. Benaouda OF, Mezaache M, Bouchakour M, Bendiabdellah A (2023) Estimation of the droplet detachment frequency using SSAS and PSD techniques in GMAW process under different transfer modes. Int J Adv Manuf Technol 126:1979–1996. https://doi.org/10.1007/s00170-023-11125-6

12. Liu HS, Xue RL, Zhou JP, Bao Y, Xu Y (2023) Applying statistical models to optimize the weld bead geometry in the vertical oscillation arc narrow gap all-position GMAW. Appl Sci 13(11):6801. https://doi.org/10.3390/app13116801

13. Guo N, Lin SB, Gao C, Fan CL, Yang CL (2009) Study on elimination of interlayer defects in horizontal joints made by rotating arc narrow gap welding. Sci Technol Weld Joining 14(6):584–588. https://doi.org/10.1179/136217109X456942

14. Ahsan MRU, Cheepu M, Ashiri R, Kim TH, Jeong C, Park YD (2017) Mechanisms of weld pool flow and slag formation location in cold metal transfer (CMT) gas metal arc welding (GMAW). Weld World 61:1275–1285. https://doi.org/10.1007/s40194-017-0512-3

15. Cai HY, Xu LY, Zhao L, Han YD, Pang HN, Chen W (2020) Cold metal transfer plus pulse (CMT+P) welding of G115 steel: mechanisms, microstructure, and mechanical properties. Mater Sci Eng A 843:143–156. https://doi.org/10.1016/j.msea.2022.143156

16. Huan PC, Wang XN, Zhang J, Hu ZR, Chen WG, Nagaumi H, Di HS (2020) Effect of wire composition on microstructure and properties of 6063 aluminium alloy hybrid synchronous pulse CMT welded joints. Mater Sci Eng A 790:139713. https://doi.org/10.1016/j.msea.2020.139713

17. Hu ZQ, Lin H, Qin XP, Ni M, Ji F, Wu MW (2021) Molten pool behaviors and forming appearance of robotic GMAW on complex surface with various welding positions. J Manuf Process 64:1359–1376. https://doi.org/10.1016/j.jmapro.2021.02.061

18. Yuan L, Pan ZX, Ding DH, He FY, Van DS, Li HJ, Li WH (2020) Investigation of humping phenomenon for the multi-directional robotic wire and arc additive manufacturing. Robot Comput Integr Manuf 63:101916. https://doi.org/10.1016/j.rcim.2019.101916

19. Guo W, Li L, Dong SY, Crowther D, Thompson A (2017) Comparison of microstructure and mechanical properties of ultra-narrow gap laser and gas-metal-arc welded S960 high strength steel. Opt Lasers Eng 91:1–15. https://doi.org/10.1016/j.optlaseng.2016.11.011

20. Yang T, Liu JF, Zhuang Y, Sun K, Chen WL (2020) Studies on the formation mechanism of incomplete fusion defects in ultranarrow gap laser wire filling welding. Opt Laser Technol 129:106275. https://doi.org/10.1016/j.optlastec.2020.106275

21. Li RY, Yue J, Sun R, Mi GY, Wang CM, Shao XY (2016) A study of droplet transfer behavior in ultra-narrow gap laser arc hybrid welding. Int J Adv Manuf Technol 87:2997–3008. https://doi.org/10.1007/s00170-016-8699-9

22. Zhang YX, Han SW, Cheon J, Na SJ, Gao XD (2017) Effect of joint gap on bead formation in laser butt welding of stainless steel. J Mater Process Technol 249:274–284. https://doi.org/10.1016/j.jmatprotec.2017.05.040

23. Han SY, Tang XH, Liu GQ, Xu LD, Cui HC, Shao CD (2022) Effects of arc interaction on lack-of-fusion and porosity in tandem NG-GMAW of 5083 Al-Mg alloy. J Manuf Process 81:92–106. https://doi.org/10.1016/j.jmapro.2022.06.059

24. Guo N, Wang MR, Wei G, Yu JB, Feng JC (2014) Study on forming mechanism of appearance defects in rotating arc narrow gap horizontal GMAW. Int J Adv Manuf Technol 75:15–20. https://doi.org/10.1007/s00170-014-6127-6

25. Lin X, Yang HO, Chen J, Huang WD (2006) Microstructure evolution of 316L stainless steel during laser rapid forming. Acta Metall Sin Chin Ed 42:361–368. https://doi.org/10.1360/crad20061117

26. Wang JY, Jiang YQ, Zhu J, Liu DS, Xu GX, Li WH (2023) Development of swing arc narrow gap GMAW process assisted by swaying wire. J Mater Process Technol 318:118004. https://doi.org/10.1016/j.jmatprotec.2023.118004

27. Fang C, Wei J, Liu J (2021) Solidification cracking sensibility of narrow gap laser welding on ITER-grade austenitic stainless steel. Fusion Eng Des 162:112068. https://doi.org/10.1016/j.fusengdes.2020.112068

28. Lippold JC, Kotecki DJ (2005) Welding Metallurgy and Weldability of Stainless Steels. John Wiley & Sons Inc., Hoboken https://doi.org/10.1080/10426910500476747

29. Yang F, Li CW, Li ZJ, Jiang L, Ye XX, Liu F (2020) Investigation on microstructure and hardness of UNS N10003 weld cladding on 316H with optimization of process parameters. Mater Sci Technol 28:1–8. https://doi.org/10.11951/j.issn.1005-0299.20180386

30. Lin X, Ren Z, Fautrelle Y, Gagnoud A, Zhang Y, Esling C (2009) Degeneration of columnar dendrites during directional solidification under a high magnetic field. Scripta Mater 60:443–446. https://doi.org/10.1016/j.scriptamat.2008.11.036

31. Kawahito Y, Mizutani M, Katayama S (2009) High quality welding of stainless steel with 10 kW high power fibre laser. Sci Technol Weld Joining 14(4):288–294. https://doi.org/10.1179/136217108X372531

32. Ravikiran K, Das G, Kumar S, Singh PK, Sivaprasad K, Ghosh M (2019) Narrow gap welding of low alloy and austenitic stainless steels using different Inconel alloys: comparison of microstructure and properties. Mater Res Express 6(9):096518. https://doi.org/10.1088/2053-1591/ab2be2

33. Hall EO (1970) Yield point phenomena in metals and alloys. Plenum Press, New York

34. Yang X, Chen H, Li MV, Bu H, Cai C (2021) Porosity suppressing and grain refining of narrow-gap rotating laser-MIG hybrid welding of 5A06 aluminum alloy. J Manuf Process 68:1100–1113. https://doi.org/10.1016/j.jmapro.2021.06.036